Advanced analysis of liquid dispersion and gas–liquid mass transfer in a bubble column with dense vertical internals

Felix Möller[a], Alan MacIsaac[a], Yuk Man Lau[a,b], Eckhard Schleicher[a], Uwe Hampel[a,c], Markus Schubert[a,]*

[a] *Institute of Fluid Dynamics, Helmholtz-Zentrum Dresden-Rossendorf, Bautzner Landstr. 400, 01328 Dresden, Germany*
[b] *Laboratory for Aero- and Hydrodynamics, Delft University of Technology, Mekelweg 2, 2628 CD Delft, The Netherlands*
[c] *AREVA Endowed Chair of Imaging Techniques in Energy and Process Engineering, Technische Universität Dresden, 01062 Dresden, Germany*

ARTICLE INFO

ABSTRACT

The influence of dense vertical tube bundles in a batch bubble column reactor (BCR) of 100 mm diameter and 1100 mm clear liquid height on liquid dispersion and gas–liquid mass transfer was studied. In particular, the effects of different tube patterns (triangular and square pitch), tube diameters (8 and 13 mm) and bottom end designs (flat and U-tube) having a tube diameter-to-pitch ratio of approx. 1.3 were investigated.

Dispersion coefficients were determined based on conductive tracer experiments recorded via wire-mesh sensors (WMS) with up to 90 measurement points distributed in the column's cross-section in between the tubes. The gas–liquid mass transfer coefficient was determined via fast-responding oxygen needle probes. Tube pitch and pattern were identified as the most crucial design parameters for the extent of liquid dispersion. We found that particularly the U-tube bottom end design induces large liquid circulation patterns, which enhance dispersion. The presence of internals decreases the $k_l a$ value as a consequence of turbulence damping, which is also confirmed by lower k_l values (e.g. 0.6×10^{-3} m s^{-1} for the empty BCR and 0.25×10^{-3} m s^{-1} for the square pitch with 8 mm tubes at 0.05 m s^{-1} superficial gas velocity), whereas the pitch is the most decisive design parameter. The U-tube bottom end design was identified as the most beneficial configuration with respect to liquid mixing and gas–liquid mass transfer.

1. Introduction

Bubble column reactors (BCRs) are preferably used for gas/liquid and gas/liquid/solid reactions, since they are easy to construct and to maintain due to the absence of moving parts. Compared to trickle bed reactors and fluidized beds, they have superior heat and mass transfer characteristics at lower energy input (Deckwer et al., 1978; Deckwer, 1992). Bubble column reactors are mainly used for oxygenation and hydrotreating processes as well as for waste water treatment, and others. Many bubble column processes, such as the Fischer–Tropsch synthesis or the methanol synthesis, involve highly exothermic reactions. Typical Fischer–Tropsch reaction conditions are $T = 200\,^\circ$C, $P = 400$ bar and $\Delta H_R = -210$ kJ mol^{-1} (Kölbel and Ackermann, 1958; Schlüter et al., 1995; Maretto and Piccolo, 1998; Casanave

---

Nomenclature

Abbreviations

ADM	Axial dispersion model
ADC	Analog-to-digital converter
BCR	Bubble column reactor
CSTR	Continuous stirred tank reactor
DM	Dispersion model

Roman symbols

a	Interfacial area, $\mathrm{m^2\,m^{-3}}$
a_1, a_2, a_3	Fitting constants, –
A_c	Coverage ratio, %
A_o	Opening sparer area ratio, %
A_s	Sub-channel area, $\mathrm{m^2}$
c^*	Equilibrium concentration, $\mathrm{mol\,m^{-3}}$
c_i	Gas or liquid concentration, $\mathrm{mol\,m^{-3}}$
c_s	Concentration at sensor, $\mathrm{mol\,m^{-3}}$
c_T	Dimensionless tracer concentration, –
d	Perforated plate hole diameter, m
d_h	Hydraulic diameter, m
d_o	Outer tube diameter, m
d_s	Sauter mean diameter, m
D	Inner column diameter, m
D_{ab}	Liquid diffusivity coefficient, $\mathrm{m^2\,s^{-1}}$
$D_{r,l}$	Radial liquid dispersion coefficient, $\mathrm{m^2\,s^{-1}}$
$D_{z,i}$	Axial dispersion coefficient for gas or liquid phase, $\mathrm{m^2\,s^{-1}}$
$D_{z,corr}$	Axial dispersion coefficient from correlation, $\mathrm{m^2\,s^{-1}}$
$D_{z,meas}$	Measured axial dispersion coefficient, $\mathrm{m^2\,s^{-1}}$
f	Electrolyte factor, –
g	Gravitational acceleration, $\mathrm{m\,s^{-2}}$
H	Henry constant, –
J_o	Zero order Bessel function, –
k_l	Mass transfer coefficient, $\mathrm{m\,s^{-1}}$
$k_l a$	Volumetric mass transfer coefficient, $\mathrm{s^{-1}}$
$k_l a_{corr}$	Mass transfer coefficient from correlation, $\mathrm{s^{-1}}$
$k_l a_{meas}$	Measured mass transfer coefficient, $\mathrm{s^{-1}}$
K_s	Sensor constant, $\mathrm{s^{-1}}$
L	Column length, m
L_c	Clear liquid height, m
L_d	Dispersed liquid height, m
L_s	Sensor height from the top of the dynamic liquid height, m
N	Number of tubes, –
p	Tube pitch, m
P	Pressure, bar
r	Radial position, m
r/R	Dimensionless radius, –
R	Inner column radius, m
t	Time, s
T	Temperature, °C
u_i	Superficial gas or liquid velocity, $\mathrm{m\,s^{-1}}$
z	Axial distance from sparger, m

Greek symbols

β	Dimensionless radius, –
ε_i	Overall holdup for liquid or gas phase, –
μ_i	Dynamic liquid or gas viscosity, Pa s
ν_m	mth root of the first-order Bessel function
ρ	Dimensionless radial position, –
ρ_i	Liquid or gas density, $\mathrm{kg\,m^{-3}}$
σ	Surface tension, $\mathrm{N\,m^{-1}}$
θ	Dimensionless time, –
ζ	Dimensionless axial position, –

et al., 1999; Maretto et al., 2002; Hensman, 2004; Hawthorne et al., 2006; Lee et al., 2009; Hugues et al., 2010). Isothermal conditions, which are essential for high product selectivity and catalyst efficiency, have to be ensured (Schlüter et al., 1995; Youssef, 2010; Youssef et al., 2013). Typically, reactor temperature is controlled via heat exchangers. In case of smaller reactors, jacket cooler devices may be used. Circulating the reaction fluid through an external heat exchanger is another option. For such, there is no fundamental size restriction but as separate components they are often more expensive. Alternatively, internal heat exchanger devices, such as horizontal or vertical tube bundles in a straight or coil-type manner, are used. However, for such, proper sealing at the reactor wall is more complicated. Hence, vertical heat exchanger tube bundles are preferred in bubble column reactors, especially in high-pressure systems (Kölbel and Ackermann, 1958; Schlüter et al., 1995; Rollbusch et al., 2015).

Typically, 20%–30% of the reactor cross-sectional area is occupied by the tube bundles (Schlüter et al., 1995; Casanave et al., 1999; Youssef et al., 2013). Recently, Möller et al. (2018) have shown that gas holdup and bubble size distribution are significantly altered, when internals are installed. Consequently, there is also an influence on gas–liquid mass transfer and liquid mixing as both depend on bubble size and bubble-induced turbulence. However, while liquid mixing as well as mass transfer in empty bubble columns have been extensively studied (Mangartz and Pilhofer, 1981; Shah et al., 1982; Krizan, 1987; Deckwer, 1992; Han, 2007; Han and Al-Dahhan, 2007), knowledge on bubble columns with heat exchanger internals is rare. In the following, we will briefly discuss the state of the art as derived from public literature.

Liquid mixing in bubble columns with internals was studied by Youssef (2010), Bernemann (1989), Forret et al. (2003) and most recently by Kalaga et al. (2017). Youssef (2010) and Bernemann (1989) operated their bubble column with a continuous liquid flow at comparably high superficial liquid velocities of up to $0.045\,\mathrm{m\,s^{-1}}$, which is known to increase the liquid dispersion coefficient. Youssef (2010) revealed that the axial dispersion coefficient of the liquid phase slightly increases with the insertion of internals. Bernemann (1989) further showed that the more tubes are inserted into the reactor and, thus, the covered area of the cross-section increases, the higher the axial dispersion coefficient, which is attributed to an enhanced formation of faster rising bubbles and steeper liquid velocity gradients in the cross-section (Bernemann, 1989; Bernemann et al., 1991; Chen et al., 1999). Similarly, Youssef (2010) obtained increasing axial dispersion coefficients for those tube layouts, which promote coalescence (e.g. circular arrangements with a free region in the column center). Shah et al. (1978) analyzed their tracer experiments in a bubble column with tube internals via the Axial Dispersion Model (ADM). Forret et al. (2003) argued that radial dispersion must not be neglected in order to properly reflect the radial tracer spreading observed with internals, which cause large circulation cells and local eddies as also confirmed by others (Larachi et al., 2006; George, 2015). Recently, Kalaga et al. (2017) used a radioactive tracing technique to study liquid mixing and measured higher liquid dispersion coefficients for the column with internals. However, they also considered axial dispersion only, which is in contrast to the results and methodology of Forret et al. (2003). To progress in the experimental analysis of effects on radial dispersion, a spatially distributed liquid tracer measurement is required.

Hitherto, the gas–liquid mass transfer in bubble columns with internals was studied by Hamed (2012) only. Hamed (2012) determined slightly lower $k_l a$ values for the column with internals. Since internals are known to dampen the turbulence intensity, as shown in several experimental studies and CFD simulations (Chen et al., 1999; Larachi et al., 2006; Laborde-Boutet et al., 2010), the k_l value should be lower, too. Hamed (2012) also observed that the $k_l a$ value is not very sensitive to variations (±20%) of the dispersion coefficients in the applied ADM.
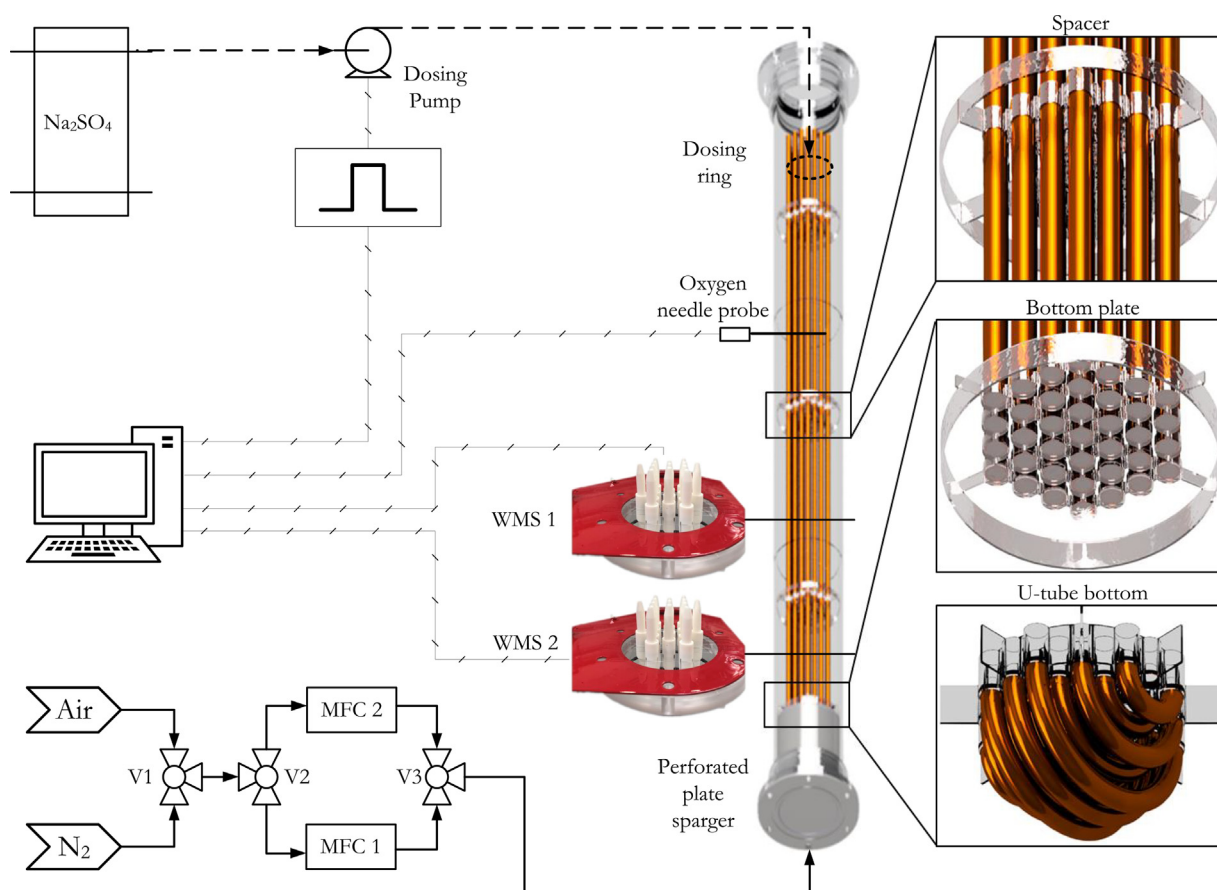
Fig. 1 – Schematic diagram of the experimental setup.

Hamed (2012) proposed the application of the ADM rather than the continuous stirred tank reactor (CSTR) model for the analysis of the mass transfer for columns with internals. However, no comprehensive mass transfer study considering the effects of various tube patterns is yet available.

The objective of the study being presented in this article was to investigate the relation between tube bundle design and gas–liquid mass transfer coefficient quantitatively and to assess if a 2D dispersion model (2D-DM) can reliably predict liquid dispersion in a bubble column with dense vertical tube internals. For that purpose, we used advanced analytical techniques, namely tailored wire-mesh sensors, for conductive tracer dispersion and fast-responding oxygen needle probes for mass transfer measurements. In addition, we used available bubble size data from earlier ultrafast X-ray tomography measurements to estimate the k_l coefficient.

2. Experimental

2.1. Bubble column setup and internal design

The experimental setup is schematically shown in Fig. 1. A bubble column with an inner diameter of 100 mm was used. The height of the column is 2000 mm and the clear liquid height was always kept at 1100 mm regardless of the installed internal. As sparging device, a perforated plate with 55 holes of 0.5 mm (free area 0.14%) arranged in a triangular pitch of 10 mm was used.

Four different internals of square and triangular pitch and with tube diameters of 8 mm and 13 mm were used. All configurations covered a similar cross-sectional area of approx. 25%, which is a common value for the Fischer–Tropsch synthesis. The specifications of the internals are summarized in Table 1. The wall zone $(0.75 < r/R \leq 1)$ was kept free of

internals as recommended by Youssef (2010) and Li and Prakash (2001) to ensure better heat removal and easier maintenance in industrial applications.
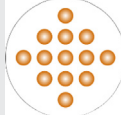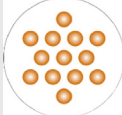
A schematic diagram of the used experimental setup as well as a CAD (Computer-Aided Design) 3D model drawing of the bubble column and its internals, showing also the spacers for alignment and fixation of the tube bundle, is given in Fig. 1. As the influence of the bottom end design has not yet been addressed in the literature, we equipped the square 8 (s8) configuration additionally with a U-tube bottom end (su8) to mimic industrial heat exchangers.
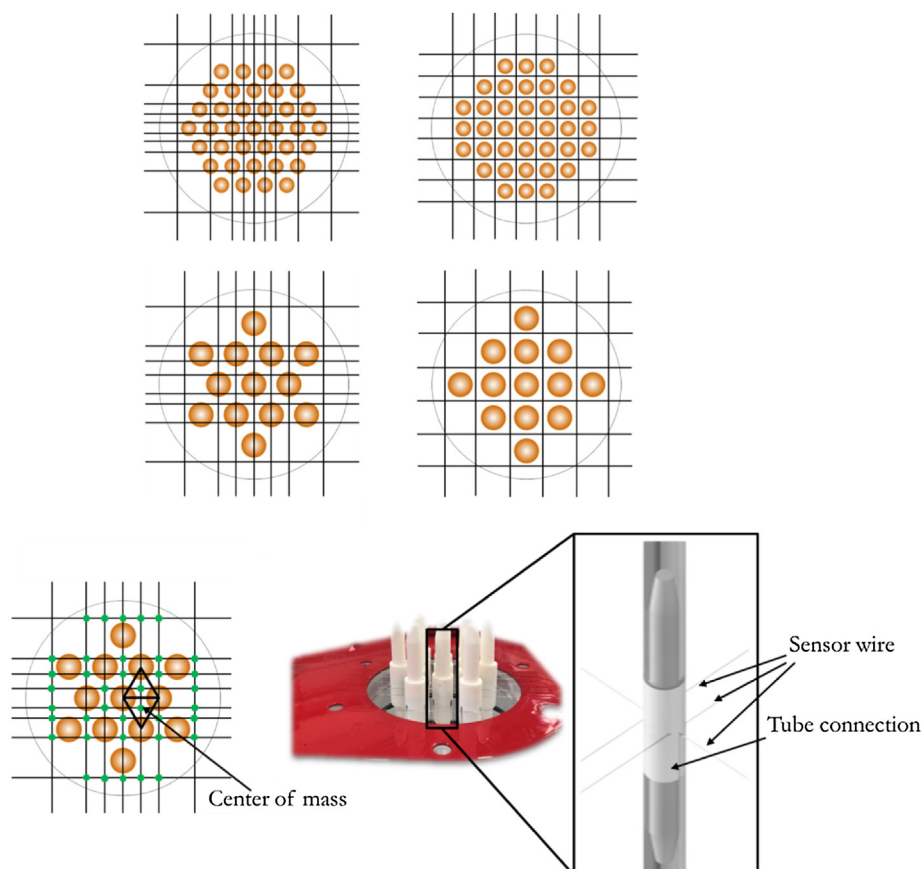
Experiments were conducted at superficial gas velocities (based on the free cross-sectional area) ranging from $0.02\,\mathrm{m\,s^{-1}}$ to $0.20\,\mathrm{m\,s^{-1}}$ adjusted via two mass flow controllers (Omega, FMA-2608A and FMA 2611A) covering homogeneous and heterogeneous flow conditions. To maintain a constant operating temperature, the gas was kept at 20 °C via a controlled heat exchanger. The functional principles and data analysis for liquid tracer concentration via WMS and oxygen concentration measurement via fast-responding needle probe are explained below. For the description of the ultrafast X-ray tomography and for the determination of bubble size data (Sauter mean diameter), the reader is referred to Möller et al. (2018) and Lau et al. (2018).

2.2. Wire-mesh sensor and liquid dispersion measurement

Dispersion is typically assessed by analyzing the spatio-temporal concentration profile of a tracer, such as a salt, heat or dye. In this study, we injected 5 mL Na_2SO_4 (sodium

Table 1 – Summary of the tube bundle layouts and their characteristic specifications.

Type	Square 8 (s8)	Triangular 8 (t8)	Square 13 (s13)	Triangular 13 (t13)
Tube diameter (d_o) in mm	8.0	8.0	13.0	13.0
Pitch (p) in mm	11.0	11.5	17.5	18.5
Hydraulic diameter (d_h) in mm	7.6	5.6	11.8	8.9
Sub-channel area (A_s) in mm^2	70.7	32.1	173.5	81.8
Coverage (A_c) in %	24	24	23	23
Number of tubes (N)	37	37	13	13

Fig. 2 – WMS electrode configurations for the different tube arrangements (top) and photography of the sensor for the triangular 13 (t13) configuration with zoomed view of an inlay that is part of the tube mockup and serves as a support for wire electrodes and a spacer for the tubes (bottom).

sulfate) solution (20 mmol L^{-1}) within a sharp 1.0 s period at the dispersed liquid height on top of the column via a dosing pump (ISMATEC ISM446, controlled by an Agilent 33250A signal generator). Sulfate salts are applicable since they do not promote corrosion of the sensor wires. Following others, e.g. Deckwer (1992) and Bloch et al. (2015), we used a perforated ring (85 mm diameter with 12 openings of 0.5 mm) on top of the column to secure a most uniform initial tracer distribution in the cross-section. For the cross-sectional tracer concentration measurement, we used wire-mesh sensors. A WMS consists of a multitude of 100 μm thick wire electrodes stretched in two adjacent planes and in perpendicular orientation across the flow cross-section. Electrodes in one plane act as electrical transmitters, whereas the ones in the other plane act as receivers. With a special excitation scheme, one can measure the electrical resistance in each crossing point of the sensor

at high speed, thus giving conductance images at high rate. More details on the WMS technique can be found elsewhere (Prasser et al., 1998; Kipping et al., 2016; Furuya et al., 2017). The sensors that have been used in this study are of a special design with at least one wire crossing point in each sub-channel of the tube bundle (e.g. sensor wires obstruct only 0.17% of the CSA). Fig. 2 exemplarily shows the WMS electrode configuration for the triangular 13 mm tube patterns. Thus, for the square patterns (s13, s8), the wires have a regular spacing, while for the triangular configurations (t8, t13), they have an irregular spacing. The crossing points, however, are always in the "center-of-mass" of the sub-channels. To guide the wires and provide support and spacing for the tubes, 3D-printed plastic inlays are foreseen (Fig. 2, bottom).

Two wire-mesh sensors were mounted at distances of $L_s/L_d = 0.9$ and 0.7 from the tracer injection at the column
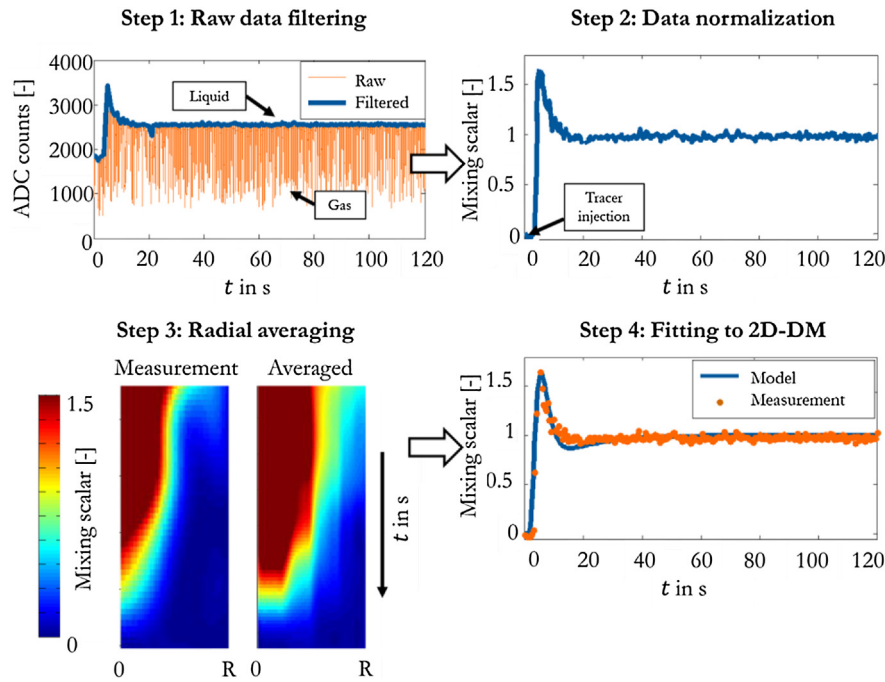
Fig. 3 – WMS data post-processing procedure and dispersion parameter extraction (data in Steps 1 and 2 shown for one virtual crossing point only, data in Step 4 shown for one radius only).

top following the suggested rule of thumb ($L_s/L_d \approx 0.8$) proposed by Deckwer (1992). That is, their absolute positions were 0.21 m and 0.46 m above the sparger. Tracer injection and measurement were simultaneously triggered via an in-house developed trigger device (Clock-Box). All tracer measurements were repeated five times. To avoid any effect on the hydrodynamics due to tracer accumulation, fresh deionized water was used for each measurement. The tracer measurements were performed at a WMS frame rate of 5000 Hz for a total scanning time of 240 s.

2.3. Oxygen probe and mass transfer measurement procedure

For measuring the mass transfer, a fast-responding needle probe sensor with a Clark electrode (Unisense OX 100) was used. Oxygen penetrates through a membrane at the sensor tip and is subsequently reduced at the cathode, which is then polarized against an internal Ag/Agl anode. The resulting current is then converted to concentrations by calibration. The needle probe was located at r/R = 0.8 (outside of the tube bundle) and a height of 0.70 m above the gas sparger (i.e. $L_c/D = 7$) to ensure fully developed flow (Wilkinson et al., 1992). At first, the column was flushed with nitrogen to fully strip the oxygen from the deionized water. Subsequently, a three way valve was switched to pressurized air. Depending on the superficial gas velocity, the measurement time varied between 60 s and 240 s until oxygen saturation was reached. Each measurement was repeated three times with the identical procedure.

According to Deckwer et al. (1983), Han and Al-Dahhan (2007) and Hamed (2012), the overall volumetric mass transfer coefficient in bubble columns depends on the degree of liquid backmixing superimposed to plug flow. Therefore, it is important to determine the mixing of the fluid phases in order to correctly determine the mass transfer coefficient by assessing the ADM model.

3. Data analysis

3.1. Extraction of the liquid dispersion coefficients

Following Forret et al. (2003), a two-dimensional dispersion model (2D-DM) was used to capture the flow behavior in the bubble column. It is described by the following equation

$$\frac{\partial c_l}{\partial t} = D_{z,l} \frac{\partial^2 c_l}{\partial z^2} - u_l \frac{\partial c_l}{\partial z} + \frac{D_{r,l}}{r} \frac{\partial c_l}{\partial r} + D_{r,l} \frac{\partial^2 c_l}{\partial r^2}. \tag{1}$$

Here, $D_{z,l}$ and $D_{r,l}$ denote the axial and radial liquid dispersion coefficients, r is the radial position in the reactor and u_l is the superficial liquid velocity (zero for batch operation). An analytical solution was derived by Rubio et al. (2004) using the Danckwert's boundary conditions (zero gradient boundary), which is

$$c_T(x, y) = \left(\sum_{m=1}^{\infty} \frac{J_0(v_m \rho)}{J_0(v_m \beta)} \cdot \exp\left(-v_m^2 \theta\right) \right)$$
$$\left(1 + 2 \sum_{n=1}^{\infty} \left[(\cos n\pi\zeta) \cdot \exp\left(-n^2\pi^2\theta\right) \right] \right). \tag{2}$$

The dimensionless parameters are defined as

$$\theta = \frac{D_{z,l}t}{L_d^2}, \zeta = \frac{z}{L_d}, \rho = \frac{r}{L_d}\sqrt{\frac{D_{z,l}}{D_{r,l}}}, \beta = \frac{R}{L_d}\sqrt{\frac{D_{z,l}}{D_{r,l}}}. \tag{3}$$

The dimensionless tracer concentration, c_T, (also called mixing scalar) depends on the dimensionless time, θ, the dimensionless axial position, ζ, and the dimensionless radial position, ρ, as well as the dimensionless radius, β. J_0 is the zero-order Bessel function and v_m is the mth root of the first-order Bessel function. If $D_{r,l} \gg D_{z,l}$, only axial dispersion determines the mixing and Eq. (2) approaches the analytical solution for the one-dimensional ADM (Ohki and Inoue, 1970).
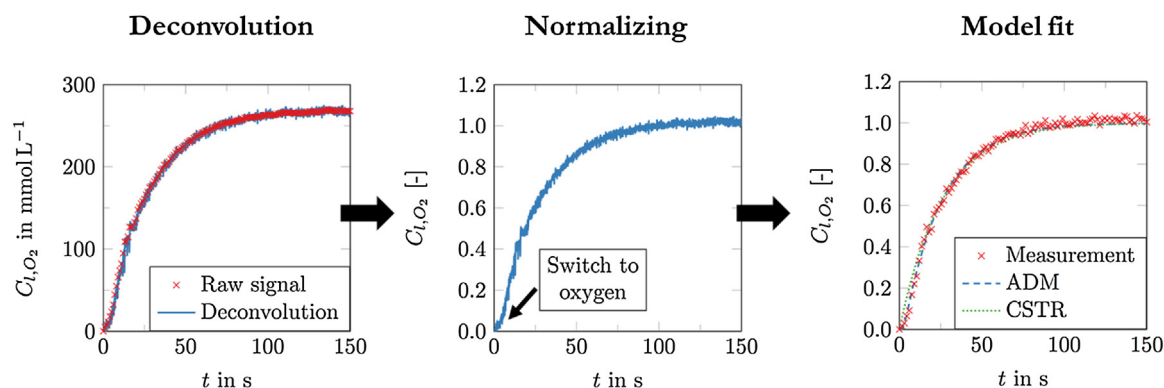
Fig. 4 – Illustration of the oxygen probe data post-processing and model fitting steps.

To calculate the mixing scalar from the WMS data, a specific WMS data post-processing procedure is applied, which is illustrated in Fig. 3. The raw signal for a single crossing point essentially follows the average local liquid conductivity but falls shortly towards zero every time a gas bubble passes the sensor crossing. Hence, we first extract the upper envelope of the curve to get rid of the gas bubble dimples (Step 1). Afterwards, the signal is scaled between zero, the value before tracer injection, and one, the value corresponding to the final steady-state tracer concentration after mixing is completed (Step 2). In Step 3, a radial averaging over the cross-sectional area is carried out. Subsequently, we determine the axial and radial dispersion coefficients that make the function in Eq. (2) fit best to the data in a least square sense (Step 4). The radial averaged measurement data can be viewed in the supplementary material.

3.2. Determination of the gas–liquid mass transfer coefficient

The data post-processing procedure applied in this study to obtain the mass transfer coefficients is illustrated in Fig. 4. At first, the raw data of the oxygen needle probe were de-convoluted using the response time constant to obtain instantaneous $k_l a$ values as described by Han and Al-Dahhan (2007). The convolution equation follows

$$\frac{dc_s}{dt} = K_s \left(c_l - c_s \right),\tag{4}$$

where c_l is the bulk concentration, c_s is the concentration measured at the sensor tip and K_s is the probe constant. This constant is determined experimentally from the first order response delay $(c_s(t) = 1 - \exp(-K_s t))$ switching the sensor from oxygen-saturated to nitrogen-saturated water. A value of $1.5\,\mathrm{s}^{-1}$ was determined for the probe time constant. Afterwards, the data were normalized (Fig. 4, middle) and subsequently, two models, namely, CSTR model (Eq. (5)) and ADM (Eq. (6)), were applied for the determination of the $k_l a$ value (Fig. 4, right) according to

$$\frac{dc_l}{dt} = \frac{k_l a}{\varepsilon_l} \left(c_l^* - c_l \right),\tag{5}$$

$$\frac{dc_g}{dt} = D_{z,g} \frac{d^2 c_g}{dz^2} - \frac{u_g}{\varepsilon_g} \frac{dc_g}{dz} - \frac{k_l a}{\varepsilon_g} \left(Hc_g - c_l \right),$$

$$\frac{dc_l}{dt} = D_{z,l} \frac{d^2 c_l}{dz^2} + \frac{k_l a}{\varepsilon_l} \left(Hc_g - c_l \right).\tag{6}$$

Here, $D_{z,g}$ and $D_{z,l}$ denote the gas and liquid axial dispersion coefficients, H is the Henry constant and c_g, c_l and c_l^* are the gas, liquid and saturated liquid oxygen concentrations. The dispersion coefficient for the liquid phase was extracted from the WMS data (see Section 3.1) and the axial gas dispersion coefficient was correlated according to Mangartz and Pilhofer (1980) as

$$D_{z,g} = 50 D^{1.5} \left(\frac{u_g}{\varepsilon_g} \right)^3.\tag{7}$$

The deconvoluted concentration measurements can be viewed in the supplementary material.

4. Results and discussion

4.1. Liquid dispersion

The axial and radial liquid dispersion coefficients were determined by fitting the transient normalized radial concentration profile to the analytical solution in Eq. (2) via a surface fit. Fig. 5 exemplarily shows the surface fit for the square 8 configuration with U-tube bottom end design (su8) at a superficial gas velocity of $0.04\,\mathrm{m\,s}^{-1}$.

The effect of the superficial gas velocity on axial and radial dispersion coefficients for the various tube bundle layouts with 8 mm (left) and 13 mm (right) tubes are shown in Figs. 6 and 7, respectively. Furthermore, results for the U-tube bottom end design as well as for the empty bubble column are shown for comparison. The error bars in Fig. 6 denote the standard deviation from the five repeated experiments. Initially, the axial dispersion coefficients show an exponential increase (solid symbols) regardless of the bundle configuration as known from other studies (Deckwer and Popović, 1973; Deckwer et al., 1973, 1974). At higher flow rates, however, the axial dispersion coefficient drops significantly. It should be noted that the Axial Dispersion Model contradicts the conditions present at slug and churn-turbulent flow obtained for superficial gas velocities above $0.08\,\mathrm{m\,s}^{-1}$ in our column (Aris, 1956; Siemes and Weiss, 1957). The results regarding flow pattern, flow structures and flow regime transition in the current setup have been published previously (Nedeltchev et al., 2017, 2018; Lau et al., 2018; Möller et al., 2018). Thus, the determined axial dispersion coefficients at these conditions have been plotted with empty symbols. Comparable results were also obtained by Ohki and Inoue (1970) for dispersion measurements in a bubble column of similar size operated with a perforated plate type sparger, where the dispersion
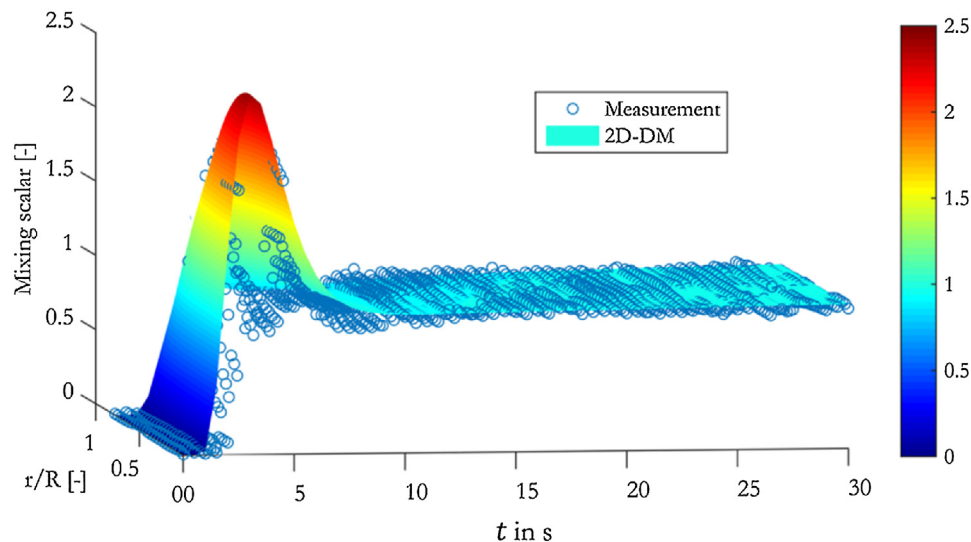
Fig. 5 – Fit of the 2D dispersion model solution to experimental data for the square 8 configuration with U-tube bottom end design (su8) at a superficial gas velocity of 0.04 m s⁻¹.
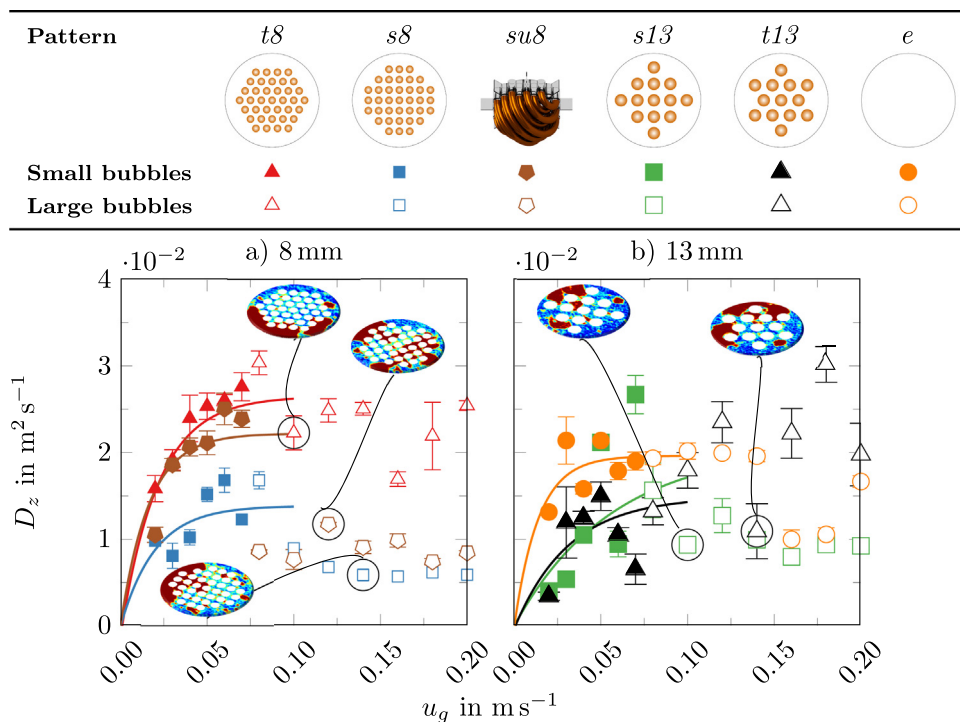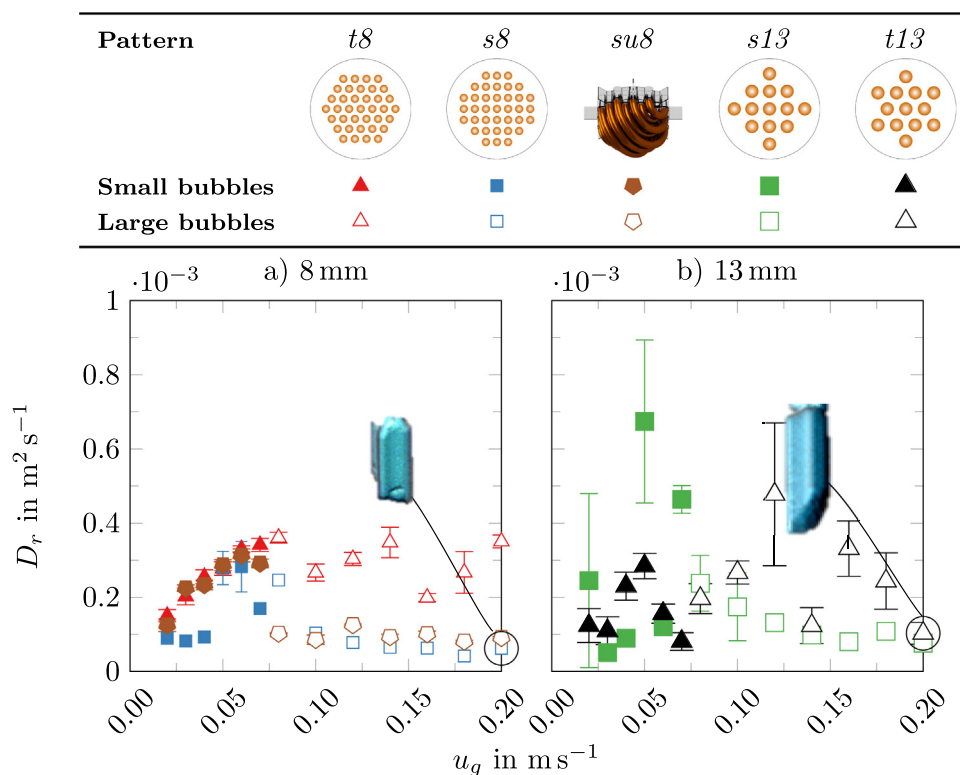

Fig. 6 – Effect of the superficial gas velocity on the liquid axial dispersion coefficient for the various tube bundles (tomographic cross-sectional images show large bubbles, indicated by dark red color, passing the measurement plane). Note that the y-axis has to be multiplied by 10⁻².

coefficient decreases at the onset of the heterogeneous flow regime. Furthermore, they found that the dispersion coefficient starts increasing again for the well-developed churn-turbulent flow regime. However, as mentioned above, the formation of large and rapidly rising bubbles in the wall zone (tomographic images exemplarily shown as inserts in Fig. 6), in particular in narrow bubble columns, where such bubbles occupy a significant ratio of the cross-section, violate the underlying homogeneous backmixing concept.

Considering the initial exponential trend for superficial gas velocities up to approx. 0.08 m s⁻¹, square 8 (s8), square 13 (s13) and triangular 13 (t13) configurations induce the lowest backmixing with dispersion coefficients similar to the empty bubble column counterpart. Here, gas bubbles are mainly

trapped within the sub-channels rising at slightly lower velocity due to interactions with the tubes. Thus, slightly lower momentum to the liquid phase is induced and accordingly, less mixing occurs. The most efficient liquid dispersion was determined for the triangular 8 (t8) configuration, which is due to the higher flow resistance caused by the pitch of the tubes and the clearly lower hydraulic sub-channel diameter of 5.6 mm. Here, the bubbles preferably rise near the wall, inducing a large-scale liquid circulation, which leads to an intensified liquid mixing. The same phenomena were observed for the U-tube bottom end structure (su8), which also forces the bubbles towards the wall.

Fig. 7 summarizes the radial dispersion coefficients for the bubble columns with internals. Again, the data for the slug and

| Pattern	t8	s8	su8	s13	t13
Small bubbles	▲	■	⬠	■	▲
Large bubbles	△	□	⬠	□	△

Fig. 7 – Radial liquid dispersion coefficient as a function of the superficial gas velocity for the various tube bundles (3D inserts show the formation of elongated bubbles in the sub-channels obtained from ultrafast X-ray tomography). Note that the y-axis has to be multiplied by 10^{-3}.

churn-turbulent flow conditions at superficial gas velocities above $0.08\,\mathrm{m\,s^{-1}}$ are only shown for the sake of completeness. The radial dispersion coefficients for the empty bubble column (not shown in Fig. 7) are up to six orders of magnitudes larger (between 1000 and $6000\,\mathrm{m^2\,s^{-1}}$), which indicates that its mixing pattern can be well described by the Axial Dispersion Model only. Compared to the axial dispersion, approx. 200 times lower coefficients were found for the radial dispersion for bubble columns with internals, which agrees with the results of Forret et al. (2003). Basically, the internals impede the radial movement of gas bubbles towards neighboring sub-channels and, hence, it is supposed that the radial liquid spreading is also suppressed. At higher throughputs, even elongated bubbles are formed, which remain encased by the sub-channel (see inserts in Fig. 7). As indicated by the lower radial dispersion coefficient, this kind of sub-channel plug flow regime seems to promote a stronger liquid confinement to the sub-channels.

However, the error bars, especially for the square and triangular 13 (t13, s13) configurations, are comparably high, which highlights the strong deviation between different measurements. As a consequence of such low radial dispersion coefficients, pronounced liquid mixing gradients occur in the column cross-section, which is a sign for large-scale axial liquid circulation and a slow radial liquid spreading (Forret et al., 2003).

4.2. Gas–liquid mass transfer, Sauter mean diameter, interfacial area

The effect of various tube patterns is comprehensively summarized below. To account for the respective backmixing behavior of the column, the mass transfer coefficient has been determined for axially dispersed and perfectly mixed liquid
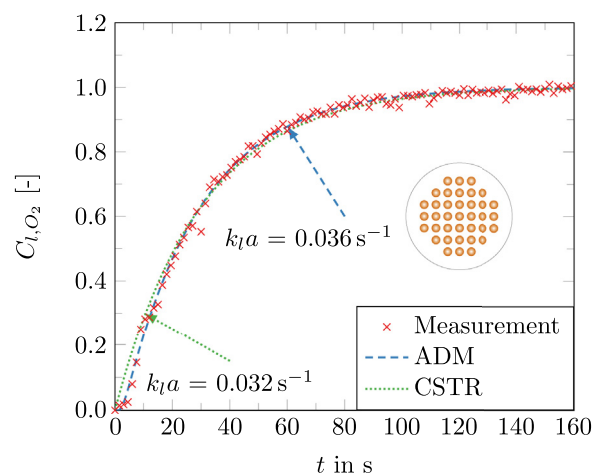
Fig. 8 – Temporal concentration profile obtained with the CSTR model and the ADM for the square 8 (s8) configuration at a superficial gas velocity of $0.02\,\mathrm{m\,s^{-1}}$.

(see Eqs. (5) and (6), respectively) as shown for the oxygen concentration in the liquid phase measured for the square 8 (s8) configuration at $u_g = 0.02\,\mathrm{m\,s^{-1}}$ (see Fig. 8). The CSTR model slightly overpredicts the initial concentration gradient, which was also confirmed by others (Han and Al-Dahhan, 2007; Hamed, 2012). The ADM, however, predicts the mass transfer curve fairly well and was, therefore, used for further analysis.

The results for the volumetric mass transfer coefficient (top row) as well as the liquid-side mass transfer coefficient (bottom row) for increasing superficial gas velocity are summarized in Fig. 9 for the smaller tubes (a) and the larger tubes as well as for the empty counterpart (b).

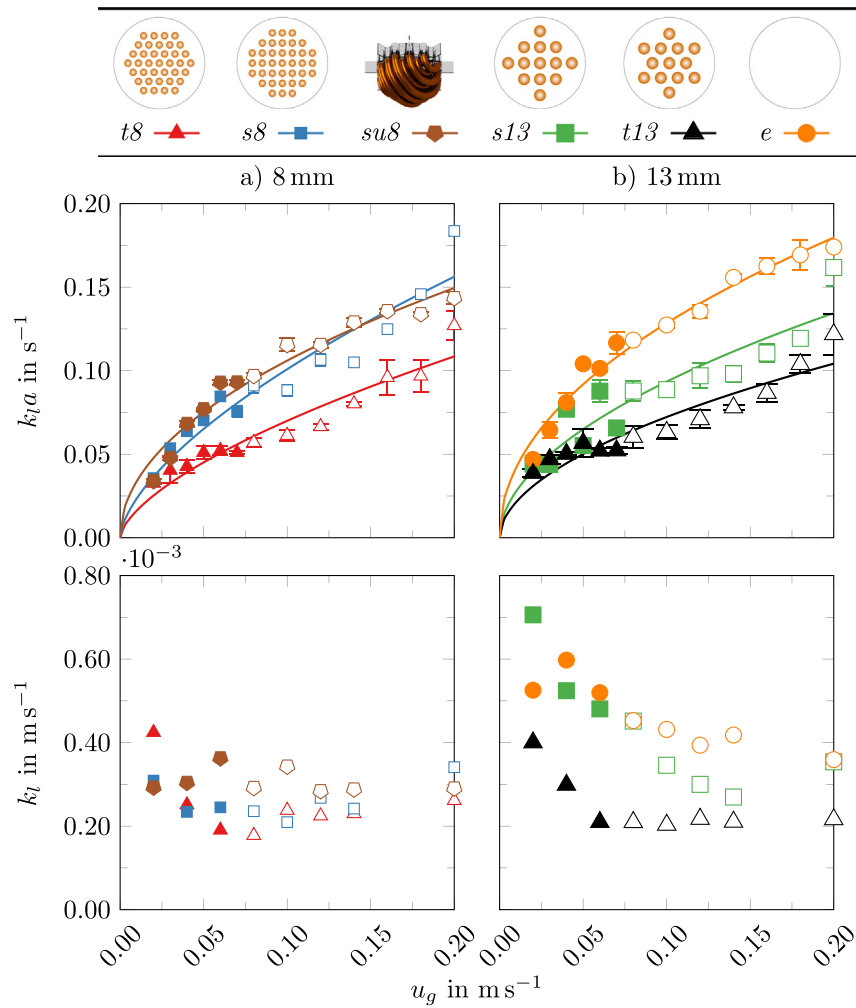**Fig. 9 – Volumetric mass transfer coefficient (top row) and liquid-side mass transfer coefficient (bottom row) as a function of the superficial gas velocity for (a) 8 mm tubes as well as the U-tube bottom end structure and (b) 13 mm tubes as well as the empty counterpart.**
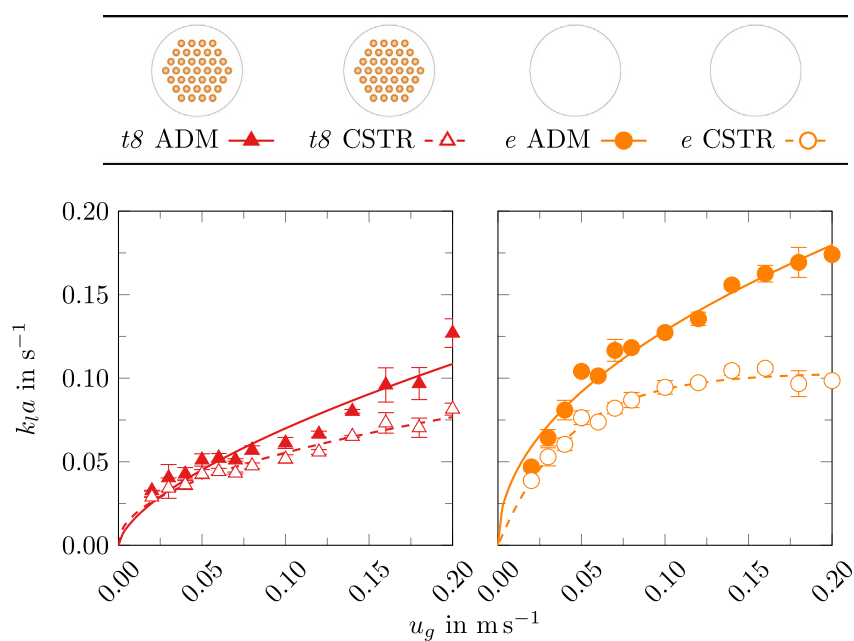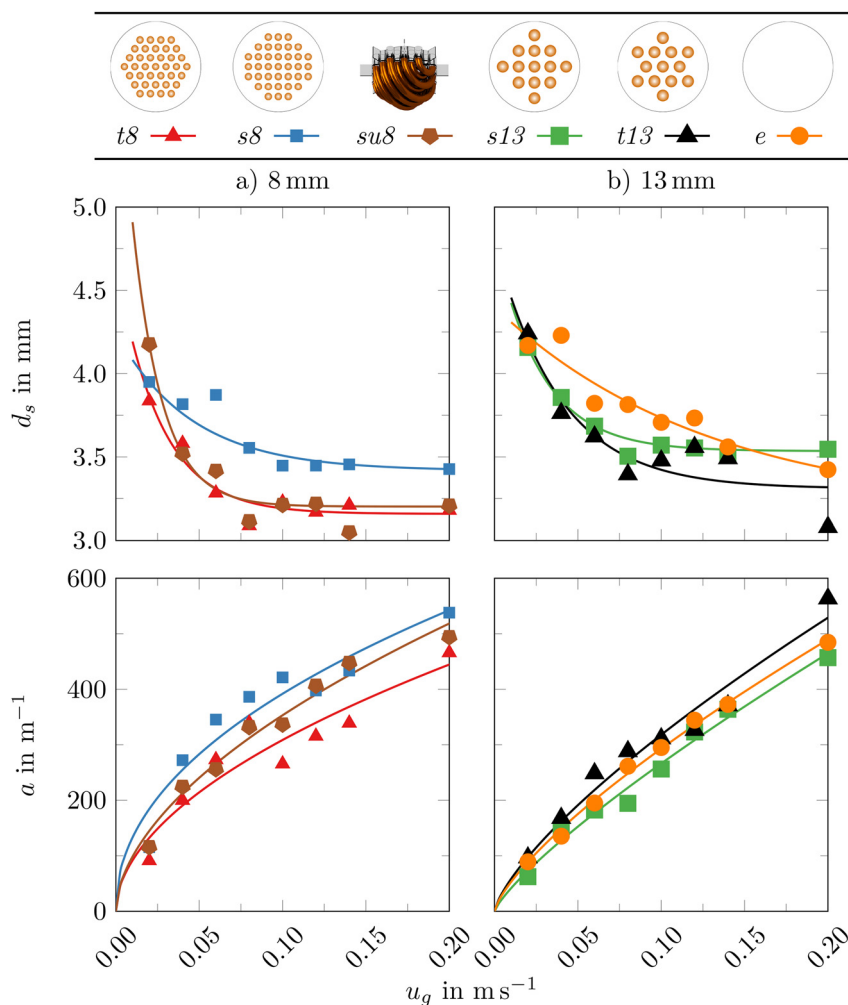

Fig. 10 – Volumetric mass transfer coefficient obtained with the ADM and the CSTR model for the BCR with internals and empty bubble column.

Fig. 11 – Sauter mean diameter (top row) and interfacial area (bottom row) as a function of the superficial gas velocity for the various internals as well as for the empty bubble column.

The volumetric mass transfer coefficient follows a power law function for all internals as well as for the empty column. The highest volumetric mass transfer coefficients were determined for the empty bubble column. This can be explained by the fact that the bubble-induced turbulence in the empty bubble column is higher due to the damping effect of the internals (Larachi et al., 2006; Laborde-Boutet et al., 2010; Hamed, 2012). The higher liquid-side mass transfer coefficient, as an indirect measure of turbulence, confirms the effect of the internals (Fig. 9, bottom row). It should be noted that the liquid-side mass transfer coefficient is calculated from the volumetric mass transfer coefficient via the specific surface area ($k_l = (k_l a)/a$) as explained below. For the internals with the 8 mm tubes smaller bubbles are formed and, hence, the interfacial area is larger compared to the empty counterpart (values for the interfacial area are shown in Fig. 11 and discussed below). This way, the larger interfacial area counterbalances the lower turbulence caused by the internals and, thus, similar volumetric mass transfer coefficients are obtained for the square 8 (s8, su8) configurations and for the empty BCR. For the larger tubes of 13 mm diameter, the interfacial area is not as large as for the smaller tubes and, hence, the volumetric mass transfer coefficient decreases. It should be noted that the liquid-side mass transfer coefficient as an indirect measure for the liquid turbulence remains nearly constant for the 8 mm tubes in the superficial gas velocity range studied, while it decreases

with increasing superficial gas velocity for the 13 mm tube configurations.

Fig. 10 illustrates the influence of the mixing model on the values of the volumetric mass transfer coefficients exemplarily for the triangular 8 (t8) tube configuration and the empty (e) BCR. For the CSTR model, the $k_l a$ values are considerably lower and the deviation between the two models increases with increasing superficial gas velocity. Especially for the empty BCR, the volumetric mass transfer coefficient is leveling off beyond 0.10 m s^{-1}, whereas the mass transfer coefficient obtained from the ADM approach is still increasing. The same trend is found for all the other configurations. Therefore, the model choice is very important as misinterpretation of the results will occur under inappropriate fluid mechanics assumptions. Hence, we suggest to always take backmixing into account.

From the tomographic imaging with the ultrafast X-ray technique, the Sauter mean diameter can be extracted as proposed by Lau et al. (2018). This supports the analysis of the mass transfer. Assuming a spherical bubble shape, the interfacial area can be calculated according to

$$a = \frac{6\varepsilon_g}{d_s},\qquad(8)$$

where ε_g is the gas holdup, which is also extracted from the X-ray measurements shown by Möller et al. (2018). However, it should be noted that some bubble diameters exceed the

Table 2 – Selected correlations for the liquid axial dispersion coefficient.		
Author	Correlation	Scope of application
Ohki and Inoue (1970)	$D_z = \frac{14D}{(1-\varepsilon_g)^2}$	$40 < D < 160$ mm $1 < u_g < 0.25$ m s^{-1}
Hikita and Kikukawa (1974)	$D_z = \left(0.015 + 0.69u_g^{0.77}\right) D^{1.25} \mu_l^{-0.12}$	$100 < D < 190$ mm $4.3 < u_g < 0.338$ m s^{-1}
Baird and Rice (1975)	$D_z = 0.35D^{1.33} g^{0.33} u_g^{0.33}$	$70.6 < D < 1520.5$ mm $0.3 < u_g < 0.45$ m s^{-1}

sub-channel diameter (e.g. due to the formation of Taylor-like bubbles as reported by Möller et al. (2018)), which will eventually lead to biased results towards slightly larger interfacial areas. However, this only holds for superficial gas velocities in the well-developed churn-turbulent flow regime.

Fig. 11 summarizes the results for Sauter mean diameter (top row) and interfacial area (bottom row). The Sauter mean diameter decreases with increasing superficial gas velocity for all configurations. This is attributed to the increasing local turbulence (Deckwer et al., 1978). Among the configurations studied, the triangular 8 (t8) configuration shows the smallest Sauter mean diameter and also the most pronounced decrease with increasing superficial gas velocity, which is attributed to the smallest sub-channel area. Furthermore, the analysis of the U-tube bottom end structure (su8) shows similar features compared to the triangular 8 (t8) configuration. The bended bottom end design promotes bubble breakup and simultaneously increases the flow resistance, which, in turn, forces the bubbles to preferably move outside the bundle. However, the influence of smaller bubbles (rising in the center of the column) outweighs the influence of large bubbles (rising in the wall region of the column). Contrary to the other configurations with 8 mm tubes, the square 8 (s8) configuration gives the largest Sauter mean diameter, which results from the larger sub-channel compared to the triangular 8 (t8) counterpart. Larger Sauter mean diameters are obtained for the larger tubes, which result from the greater sub-channel area. It can be concluded that the sub-channel area and/or the hydraulic sub-channel diameter decide on the Sauter mean bubble diameter. For the empty counterpart, however, the Sauter mean diameter is always the highest, confirming that bubble breakup is the prevailing mechanism for bubble columns with internals.

Regarding the interfacial area, a similar trend is observed. The highest interfacial area is created for the square 8 (s8) configuration, which is due to the higher gas holdup (Möller et al., 2018). This higher holdup is attributed to the additional tube wall friction acting on the bubbles, which lowers the bubble rise velocity. The interfacial area for the square 13 (s13) configuration is the lowest resulting from both the comparably low holdup as well as the larger Sauter mean diameter. However, the influence of tube size is well-pronounced as the highest interfacial area is obtained for smaller tubes, which results from a smaller hydraulic sub-channel diameter. The differences between the larger tubes and the empty BCR are almost negligible.

4.3. Literature comparison

This section aims on comparing the axial dispersion coefficients and the volumetric mass transfer coefficients from this study with available literature correlations.

4.3.1. Comparison of the axial dispersion coefficient with selected correlations

To the best of our knowledge, no correlation for the axial dispersion coefficient is currently available for bubble columns with internals. Thus, correlations originally developed for empty bubble columns of similar dimensions and operating conditions were used for comparison (see Table 2). The correlation of Ohki and Inoue (1970) was developed for the so-called coalesced bubble-slug flow to assess the influence of larger bubbles on the liquid dispersion coefficient. Accounting for various liquids and different column diameters, Hikita and Kikukawa (1974) developed a correlation taking the liquid viscosity into account. The correlation of Baird and Rice (1975) was developed based on a theoretical approach from Kolmogoroff's theory of isotropic turbulence.

It should be mentioned that the correlations are based on measurements with a single probe located at the center of the column, whereas the experiments of this paper also consider the radial tracer dispersion within the cross-section.

Fig. 12 compares the measured axial dispersion coefficients from this study with predictions of available correlations by means of parity plots. The correlations apply fairly well for the empty BCR (orange symbols), however, the predictions for the column with internals show considerable deviations as funneling effects as well as overlapping of small and large-scale circulations are not considered in the current state of the art. The current way of using global liquid dispersion data is certainly not suitable to cope with different configurations of the internals. Thus, in the future, new correlations for columns with internals should include geometry terms considering the bundle design. However, a larger database is required for such development, which should incorporate the influence of mixing patterns from pilot scale as well as narrow columns and the influence of internals size as well as the tube pattern.

4.3.2. Comparison of the volumetric gas–liquid mass transfer coefficient with selected correlations

Similarly, mass transfer correlations for columns with internals are not yet available. Thus, the most common correlations, originally developed for empty columns with similar dimensions, were used for comparison (Table 3). It is important to mention that the correlation developed by Schumpe et al. (1987) was derived from experimental data under the assumption of liquid backmixing (ADM), while the others assume completely mixed phases. It is also important to note that the correlations of Letzel et al. (1999) and Jordan et al. (2002) consider the gas holdup only. For comparison, holdup data obtained from the tomographic imaging were considered (Möller et al., 2018).

Fig. 13 shows the parity plots between the measurement data from this study and the predicted values from the
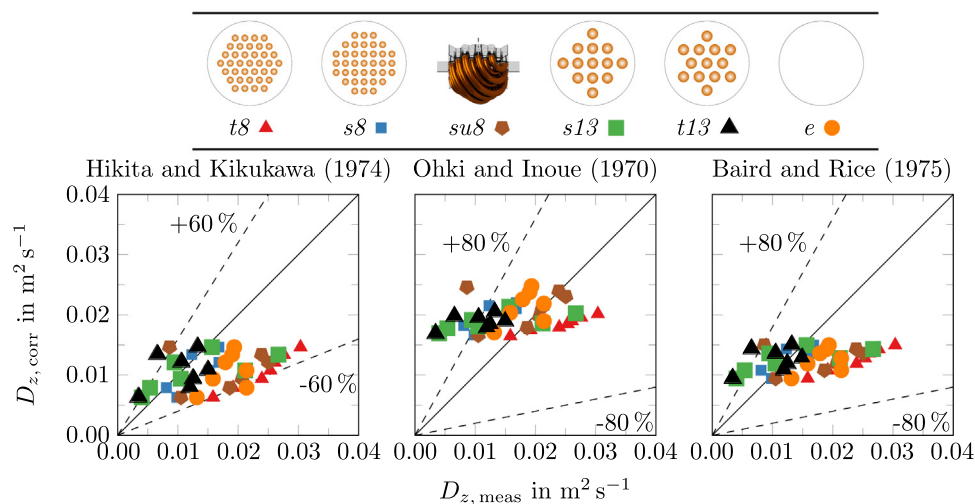
Fig. 12 – Parity plots comparing axial dispersion coefficients from this study with predictions of available correlations for superficial gas velocities up to 0.08 m s⁻¹.
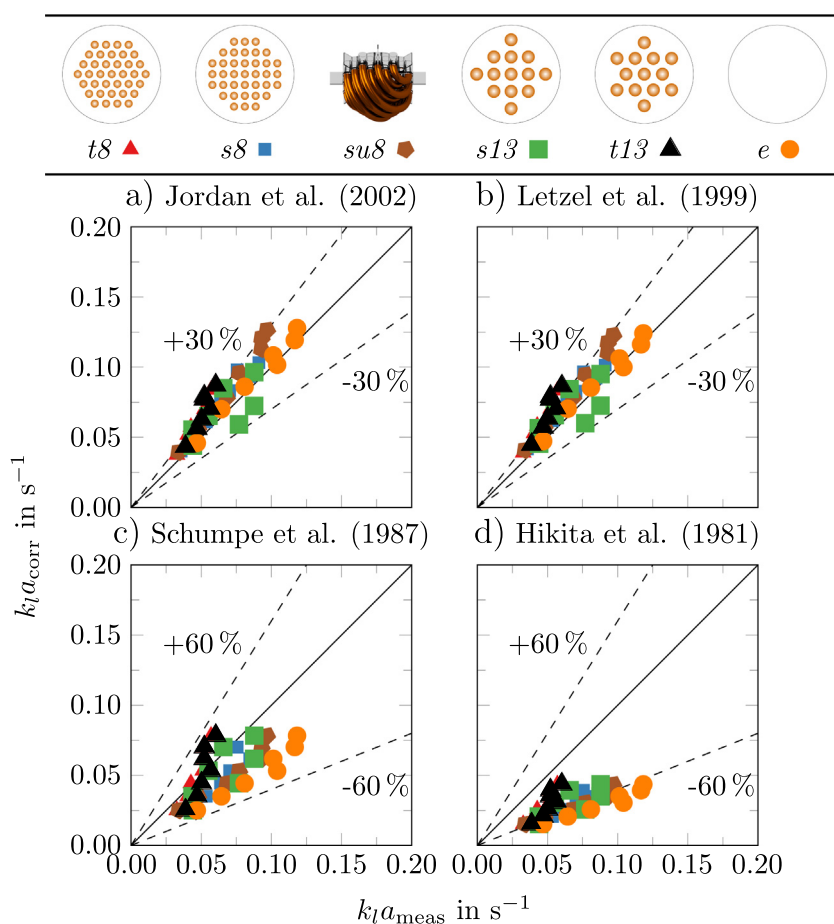

Fig. 13 – Parity plots comparing volumetric gas–liquid mass transfer coefficients from this study with predictions of available correlations from (a) Jordan et al. (2002) (b) Letzel et al. (1999) (c) Schumpe et al. (1987) and (d) Hikita et al. (1981).

correlations for the volumetric gas–liquid mass transfer coefficients. Fair agreement is obtained for the empty bubble column applying the correlations from Jordan et al. (2002) and Letzel et al. (1999). The larger deviations obtained from the correlation of Hikita et al. (1981) is probably attributed to the perfectly mixed liquid phase behavior assumed for the calculation of the volumetric mass transfer. Furthermore, single nozzle gas distributors were applied by Hikita et al.

(1981), which is known to limit the gas–liquid mass transfer due to lower gas holdup and larger gas bubbles (Han and Al-Dahhan, 2007; Möller et al., 2017). Although the correlations were developed for empty BCRs, the correlations of Letzel et al. (1999) and Jordan et al. (2002) are suitable to account for internals since the gas holdup reflects the impact of the internals. Therefore, these correlations maybe promising starting points for future work.

Table 3 – Selected correlations for the gas–liquid mass transfer coefficient.

Author	Correlation	Scope of application
Hikita et al. (1981)	$k_la = 14.9 \frac{gf}{u_g} \cdot \left(\frac{u_g\mu_l}{\sigma}\right)^{1.76} \cdot \left(\frac{\mu_l^4 g}{\rho_l\sigma^3}\right)^{-0.248} \cdot \left(\frac{\mu_g}{\mu_l}\right)^{0.243} \cdot \left(\frac{\mu_l}{\rho_l D_{ab}}\right)^{-0.604}$	$100 < D < 190\,\text{mm}$ $4.2 < u_g < 0.38\,\text{m s}^{-1}$
Schumpe et al. (1987)	$k_la = 0.042 u_g^{0.82} \mu_l^{-0.39}$	$D = 95\,\text{mm}$ $0 < u_g < 0.10\,\text{m s}^{-1}$
Letzel et al. (1999)	$k_la = 0.5\varepsilon_g$	$D = 150\,\text{mm}$ $0 < u_g < 0.40\,\text{m s}^{-1}$
Jordan et al. (2002)	$k_la = 0.56\varepsilon_g^{1.06}$	$D = 115\,\text{mm}$ $1 < u_g < 0.15\,\text{m s}^{-1}$

5. Conclusion

A comprehensive study on the influence of internals with various tube diameters (8 mm and 13 mm), layouts (square and triangular) and bottom end structures (U-tube and flat bottom end) on liquid mixing and volumetric gas–liquid mass transfer has been performed. For the first time, axial and radial dispersion coefficients for the liquid phase were extracted via a two-dimensional dispersion model from distributed tracer concentration profiles measured with embedded coarse wire-mesh sensors. In addition, the mass transfer coefficients were extracted based on the measured dissolved oxygen concentration via fast-responding probes. The main findings of this study can be summarized as follows:

- While the axial dispersion is the prevailing mixing mechanism in empty bubbles columns, radial dispersion is not negligible in bubble columns with internals. The limited radial exchange of liquid is attributed to the flow confining effect of the internals. Accordingly, the liquid spreading is much lower in the lateral direction expressed in terms of low radial dispersion coefficients.
- Amongst all internals studied, the triangular 8 (t8) configuration provides the highest axial dispersion coefficients. Here, the comparably small hydraulic diameter of the sub-channels induce a large flow resistance forcing the bubbles to preferably rise outside the bundle near the column wall promoting mixing via large scale liquid circulation. Similar trends were found for the U-tube bottom end design, where bubbles coalesce underneath and rise near the wall.
- Compared to the empty bubble column, lower volumetric gas–liquid mass transfer coefficients are obtained for columns with internals, which refers to the turbulence suppressing effect.
- Mass transfer correlations depending on the overall gas holdup show good agreement for the measurements with internals. However, axial liquid dispersion coefficient correlations fail in capturing the effect of internals.

Acknowledgement

References

Aris, R., 1956. On the dispersion of a solute in a fluid flowing through a tube. Proc. R. Soc. Lond. A: Math. Phys. Eng. Sci. 235, 67–77.

Baird, M.H.I., Rice, R.G., 1975. Axial dispersion in large unbaffled columns. Chem. Eng. J. 9, 171–174.

Bernemann, K., 1989. Zur Fluiddynamik und zum Vermischungsverhalten der flüssigen Phasen in Blasensäulen mit längsangeströmten Rohrbündeln. In: PhD Thesis. Technische Universität Dortmund, Germany.

Bernemann, K., Steiff, A., Weinspach, P.-M., 1991. Zum Einfluß von längsangeströmten Rohrbündeln auf die großräumige Flüssigkeitsströmung in Blasensäulen. Chem. Ing. Tech. 63, 76–77.

Bloch, G., Zander, H.-J., Wunderlich, B., Acher, T., 2015. Axial and radial dispersion in a large-diameter bubble column reactor at low height-to-diameter ratios. Chem. Ing. Tech. 87, 756–761.

Casanave, D., Galtier, P., Viltard, J.C., 1999. Process and apparatus for operation of a slurry bubble column with application to the Fischer-Tropsch synthesis.

Chen, J., Li, F., Degaleesan, S., Gupta, P., Al-Dahhan, M.H., Dudukovic, M.P., Toseland, B.A., 1999. Fluid dynamic parameters in bubble columns with internals. Chem. Eng. Sci. 54, 2187–2197.

Deckwer, W., Graeser, U., Langemann, H., Serpemen, Y., 1973. Zones of different mixing in the liquid phase of bubble columns. Chem. Eng. Sci. 28, 1223–1225.

Deckwer, W.-D., Nguyen-Tien, K., Kelkar, B.G., Shah, Y.T., 1983. Applicability of axial dispersion model to analyze mass transfer measurements in bubble columns. AIChE J. 29, 915–922.

Deckwer, W., Popović, M., 1973. Berechnung axial-durchmischter Rohrreaktoren als Rührkesselkaskaden mit Rücklauf. Chem. Ing. Tech. 45, 984–990.

Deckwer, W.D., 1992. Bubble Column Reactors. John Wiley & Sons Inc.

Deckwer, W.-D., Adler, I., Zaidi, A., 1978. A comprehensive study on CO2-interphase mass transfer in vertical cocurrent and countercurrent gas-liquid flow. Can. J. Chem. Eng. 56, 43–55.

Deckwer, W.-D., Burckhart, R., Zoll, G., 1974. Mixing and mass transfer in tall bubble columns. Chem. Eng. Sci. 29, 2177–2188.

Forret, A., Schweitzer, J.-M., Gauthier, T., Krishna, R., Schweich, D., 2003. Liquid dispersion in large diameter bubble columns, with and without internals. Can. J. Chem. Eng. 81, 360–366.

Furuya, M., Kanai, T., Arai, T., Takiguchi, H., Prasser, H.-M., Hampel, U., Schleicher, E., 2017. Three-dimensional velocity vector determination algorithm for individual bubble identified with Wire-Mesh Sensors. Nucl. Eng. Des., http://dx.doi.org/10.1016/j.nucengdes.2017.06.022.

George, K.J.H., 2015. Investigations in hydrodynamics and mixing pattern in the bubble column equipped with internals. In: M.Sc. Thesis. University of Western Ontario, Canada.

Hamed, M., 2012. Hydrodynamics mixing and mass transfer in bubble columns with internals. In: PhD Thesis. Washington University, St. Louis, USA.

Han, L., 2007. Hydrodynamics back-mixing and mass transfer in a slurry bubble column. In: PhD Thesis. Washington University, St. Louis, USA.

Han, L., Al-Dahhan, M.H., 2007. Gas-liquid mass transfer in a high pressure bubble column reactor with different sparger designs. Chem. Eng. Sci. 62, 131–139.

Hawthorne, W.H., Ibsen, M.D., Pedersen, P.S., Bohn, M.S., 2006. Fischer-Tropsch slurry reactor cooling tube arrangement. Patent No: US7108835B2.

Hensman, J., 2004. Fischer-Tropsch process. Patent No: US20040014825A1.

Hikita, H., Asai, S., Tanigawa, K., Segawa, K., Kitao, M., 1981. The volumetric liquid-phase mass transfer coefficient in bubble columns. Chem. Eng. J. 22, 61–69.

Hikita, H., Kikukawa, H., 1974. Liquid-phase mixing in bubble columns: effect of liquid properties. Chem. Eng. J. 8, 191–197.

Hugues, F., Szymkowiak, B., Viguie, J.C., Schweitzer, J.M., Munier, M., Chretien, D., Caprani, E., Douziech, D., 2010. Internal exchanger for gas-liquid-solid reactor for Fischer-Tropsch synthesis.

Jordan, U., Terasaka, K., Kundu, G., Schumpe, A., 2002. Mass transfer in high-pressure bubble columns with organic liquids. Chem. Eng. Technol. 25, 262–265.

Kalaga, D.V., Yadav, A., Goswami, S., Bhusare, V., Pant, H.J., Dalvi, S.V., Joshi, J.B., Roy, S., 2017. Comparative analysis of liquid hydrodynamics in a co-current flow-through bubble column with densely packed internals via radiotracing and Radioactive Particle Tracking (RPT). Chem. Eng. Sci. 170, 332–346.

Kipping, R., Brito, R., Scheicher, E., Hampel, U., 2016. Developments for the application of the Wire-Mesh Sensor in industries. Int. J. Multiph. Flow 85, 86–95.

Kölbel, H., Ackermann, P., 1958. Apparatus for carrying out gaseous catalytic reactions in liquid medium.

Krizan, P., 1987. Analyse des dynamischen Verhaltens disperser Mehrphasensysteme bei ausgeprägter Großraumströmung am Beispiel einer Gegenstrom-Blasensäule. In: PhD Thesis. Technische Universität Dortmund, Germany.

Laborde-Boutet, C., Larachi, F., Dromard, N., Delsart, O., Béliard, P.-E., Schweich, D., 2010. CFD simulations of hydrodynamic/thermal coupling phenomena in a bubble column with internals. AIChE J. 56, 2397–2411.

Larachi, F., Desvigne, D., Donnat, L., Schweich, D., 2006. Simulating the effects of liquid circulation in bubble columns with internals. Chem. Eng. Sci. 61, 4195–4206.

Lau, Y.M., Möller, F., Hampel, U., Schubert, M., 2018. Ultrafast X-ray tomographic imaging of multiphase flow in bubble columns — Part 2: characterisation of bubbles in the dense regime. Int. J. Multiph. Flow, http://dx.doi.org/10.1016/j.ijmultiphaseflow.2018.02.009.

Lee, H.T., Jung, H., Chun, D.H., Kim, H.J., Yang, J.I., Yang, J.H., 2009. A cooling system for elimination of heat of reaction at Fischer-Tropsch slurry bubble column reactor.

Letzel, H.M., Schouten, J.C., Krishna, R., van den Bleek, C.M., 1999. Gas holdup and mass transfer in bubble column reactors operated at elevated pressure. Chem. Eng. Sci. 54, 2237–2246.

Li, H., Prakash, A., 2001. Survey of heat transfer mechanisms in a slurry bubble column. Can. J. Chem. Eng. 79, 717–725.

Mangartz, K.-H., Pilhofer, T., 1980. Untersuchungen zur Gasphasendispersion in Blasensäulenreaktoren. Verfahrenstechnik (Mainz) 14, 40–44.

Mangartz, K.-H., Pilhofer, T., 1981. Interpretation of mass transfer measurements in bubble columns considering dispersion of both phases. Chem. Eng. Sci. 36, 1069–1077.

Maretto, C., Piccolo, V., 1998. Fischer-Tropsch process with a multistage bubble column reactor.

Maretto, C., Piccolo, V., Viguie, J.C., Ferschneider, G., 2002. Fischer-Tropsch process. Patent No: US6348510B1.

Möller, F., Lau, Y.M., Seiler, T., Hampel, U., Schubert, M., 2018. A study on the influence of the tube layout on sub-channel hydrodynamics in a bubble column with internals. Chem. Eng. Sci. 179, 265–283.

Möller, F., Seiler, T., Lau, Y.M., Weber, M., Weber, M., Hampel, U., Schubert, M., 2017. Performance comparison between different sparger plate orifice patterns: hydrodynamic investigation using ultrafast X-ray tomography. Chem. Eng. J. 316, 857–871.

Nedeltchev, S., Möller, F., Hampel, U., Schubert, M., 2018. Flow regime transitions in a bubble column with internals based on a novel approach. Chem. Eng. J. Jpn., http://dx.doi.org/10.1252/jcej.17we292.

Nedeltchev, S., Möller, F., Schubert, M., 2017. Effect of heat exchanger internals on the main transition velocities in a bubble column. Proceeding Third International Symposium Multiscale Multiphase Process Engineering (MMPE).

Ohki, Y., Inoue, H., 1970. Longitudinal mixing of the liquid phase in bubble columns. Chem. Eng. Sci. 25, 1–16.

Prasser, H.-M., Böttger, A., Zschau, J., 1998. A new electrode-mesh tomograph for gas-liquid flows. Flow Meas. Instrum. 9, 111–119.

Rollbusch, P., Bothe, M., Becker, M., Ludwig, M., Grünewald, M., Schlüter, M., Franke, R., 2015. Bubble columns operated under industrially relevant conditions — current understanding of design parameters. Chem. Eng. Sci. 126, 660–678.

Rubio, F.C., Mirón, A.S., García, M.C.C., Camacho, F.G., Grima, E.M., Chisti, Y., 2004. Mixing in bubble columns: a new approach for characterizing dispersion coefficients. Chem. Eng. Sci. 59, 4369–4376.

Schlüter, S., Steiff, A., Weinspach, P.-M., 1995. Heat transfer in two- and three-phase bubble column reactors with internals. Chem. Eng. Process.: Process Intensif. 34, 157–172.

Schumpe, A., Saxena, A.K., Fang, L.K., 1987. Gas/liquid mass transfer in a slurry bubble column. Chem. Eng. Sci. 42, 1787–1796.

Shah, Y.T., Kelkar, B.G., Godbole, S.P., Deckwer, W.-D., 1982. Design parameters estimations for bubble column reactors. AIChE J. 28, 353–379.

Shah, Y.T., Ratway, C.A., McIlvried, H.G., 1978. Back-mixing characteristics of a bubble column with vevertical suspended tubes. Trans. Inst. Chem. Eng. 56, 107–112.

Siemes, W., Weiss, W., 1957. Flüssigkeitsdurchmischung in engen Blasensäulen. Chem. Ing. Tech. 29, 727–732.

Wilkinson, P.M., Spek, A.P., van Dierendonck, L.L., 1992. Design parameters estimation for scale-up of high-pressure bubble columns. AIChE J. 38, 544–554.

Youssef, A.A., 2010. Fluid dynamics and scalue-up of bubble columns with internals. In: PhD Thesis. Washington Unversity, St. Louis, USA.

Youssef, A.A., Al-Dahhan, M.H., Duduković, M.P., 2013. Bubble columns with internals: a review. Int. J. Chem. React. Eng. 11, 169–223.